Electronic and hyperbolic dielectric properties of ZrS_2/HfS_2 heterostructures

Liwei Zhang,[1] Weiyang Yu,[1] Qin Wang,[1] Jun-Yu Ou,[2] Baoji Wang,[1,3] Gang Tang,[4] Xingtao Jia,[1] Xuefeng Yang,[1] Guodong Wang,[1] and Xiaolin Cai[1,*]

[1]*School of Physics and Electronic Information Engineering, Henan Polytechnic University, Jiaozuo, Henan 454000, People's Republic of China*

[2]*Optoelectronics Research Centre & Centre for Photonic Metamaterials, University of Southampton, Southampton SO17 1BJ, United Kingdom*

[3]*School of Physics Science and Engineering, Tongji University, Shanghai 200092, People's Republic of China*

[4]*Theoretical Materials Physics, CESAM, Université de Liège, B-4000 Liège, Belgium*

(Received 1 June 2019; published 22 October 2019)

In this paper we investigate the electronic and optical dielectric properties of lateral and vertical heterostructures composed of two-dimensional (2D) ZrS_2 and HfS_2 monolayers based on density-functional theory. First, we show that the bulk and monolayer ZrS_2 and HfS_2 as well as the vertical $(ZrS_2)_m/(HfS_2)_n$ heterostructures are indirect band-gap semiconductors, while the lateral heterostructures exhibit an indirect to direct band-gap transition. Then we demonstrate that the optical properties of the bulk and monolayer HfS_2 and ZrS_2 are strongly anisotropic; for the bulk HfS_2 and ZrS_2, the in-plane components of the dielectric function are negative in a certain frequency band, where they can work as naturally hyperbolic metamaterials. Interestingly, the vertical heterostructures also possess a hyperbolic region, whose position and width can be tunable with the thickness ratio of constituents. It is also found that the $(ZrS_2)/(HfS_2)$ vertical heterostructures can enhance spontaneous emission and about 100-fold improvement of the Purcell factor is obtained. These results prove the feasibility of 2D material heterostructures to realize tunable hyperbolic metamaterials; the heterostructures present a promising opportunity for the practical applications in light-generation technologies.

DOI: 10.1103/PhysRevB.100.165304

I. INTRODUCTION

Two-dimensional (2D) materials, such as graphene, hexagonal boron nitride (*h*-BN), and the transition-metal dichalcogenides (TMDs) are presently being intensively researched because of their remarkable electronic, optical, mechanical, and thermal properties [1–4]. Particularly, bulk TMDs, with the chemical formula MX_2 (M = Ti, Zr, Hf, Mo, or W; X = S, Se, or Te), are a class of important layered materials, in which transition-metal atom M and chalcogen atoms X form X-M-X–type sandwich layers by strong intralayer chemical bonding and much weaker interlayer van der Waals (vdW)-type interactions [5]. 2D monolayer TMDs display a rich physics and hold promise for a wide range of applications in flexible electronics, optoelectronics, energy storage, catalysis, or spintronics [1,4,6]. At low temperature, some monolayer TMDs can be a 2D superconductor with coexisting charge-density wave [7]. In recent years, a variety of heterostructures have also been fabricated through the vertical or lateral combination of single-layer or multilayer TMDs with other TMDs or with other 2D materials such as *h*-BN or graphene [2,8–11]. TMDs-based heterostructures assembled for various electronic, optoelectronic, and photovoltaic applications have been theoretically and experimentally studied [12,13]. Some 2D heterostructured electrodes could greatly expand current energy-storage technologies [12], while TMDs-based heterostructures such as black phosphorus/TMDs have been predicted to be strong absorbers of light and suitable materials for excitonic thin-film solar-cell applications [13]. Recently fabricated zirconium disulfide (ZrS_2) and hafnium disulfide (HfS_2) exhibit well-balanced carrier mobility and band gaps, and attracted interest in solar cells and field-effect transistors [14–16]. Meanwhile, they show highly anisotropic mechanical, optical, and electrical properties [5,17]. More importantly, the layered TMDs can be naturally hyperbolic materials (HMMs) [18].

Hyperbolic metamaterials usually have negative permittivity in at least one direction; electromagnetic waves propagating through them undergo a transition from closed elliptical to open hyperbolic dispersions in corresponding frequency [19,20]. The hyperbolic dispersion enables unique metamaterial states with large-magnitude wave vectors which are evanescent and decay exponentially in conventional media. As a matter of fact, HMMs offer great flexibility in tailoring the near-field distribution, which facilitates prospective applications in spontaneous emission enhancement [21], subwavelength imaging [20], and broadband absorption [22]. In particular, the important consequence of unbounded dispersion of HMM is a divergent local density of photonic states, which results in an enhancement in the spontaneous emission of a dipole emitter placed in the vicinity of HMM and that leads to a HMM-based broadband Purcell effect [23]. HMMs can be realized at optical frequencies using periodically arranged metal-dielectric multilayers and metallic nanowire arrays, where the unit cells are much smaller than

*caixiaolin@hpu.edu.cn

the operation wavelength [24]. However, the performance of the metal-based HHM is limited by the finite size of the metallic components. Recently, a few 2D materials have been reported to exhibit hyperbolic dispersion in their pristine form. 2D materials such as Bi_2Te_3 [25], *h*-BN [26], while graphite [27], black phosphorene [28], as well as ZrS_2 and HfS_2 [5] present hyperbolic dispersion in the UV and near-IR to visible spectral ranges. Naturally hyperbolic materials, composed of "individual layers" on the atomic scale, have been seen to curtail the limitations of the finite size of the unit cell prevalent in artificial hyperbolic structures. Containing no internal interfaces for the electrons to scatter off, they possess an obvious advantage over traditional metamaterials. In experiments, single or few-layer nanosheets of these TMDs can be obtained by using Scotch-tape-based micromechanical cleavage [29], chemical vapor deposition method, etc. [2]. In addition, many fabrication methods can be used to realize the lateral and vertical heterostructures as reviewed in Refs. [2,30]. In this paper we investigate the electronic and the tunable hyperbolic optical property of the periodic lateral and vertical heterostructures composed of single or multilayer ZrS_2 and HfS_2 based on density-functional theory (DFT). Finally, the spontaneous emission enhancement of the heterostructure-based HMMs is also calculated.

II. MODELS AND COMPUTATIONAL DETAILS

Considering the particularity of the 2D structures, there are two approaches for creating 2D heterostructures: the vertical (out of plane) and lateral (in plane) types. In this paper, we present a theoretical study of lateral and vertical heterostructures made of nearly lattice matched single or multilayer 1*T*-ZrS_2 and 1*T*-HfS_2. 1*T*-ZrS_2 and 1*T*-HfS_2 are types of 2D TMDs, which have the CdI_2 structure with $p\bar{3}m1$ space group. The vertical type, also known as vdW heterostructure, is commonly achieved by stacking multiple monolayers vertically layer by layer [31]. In contrast to the vertical heterostructures (VHs), the interfaces in lateral heterostructures (LHs) are reduced from 2D to one dimension (1D), finally becoming an "interline" [32]. The periodically repeating, lateral, and commensurate junctions of semiconducting ZrS_2 and HfS_2 stripes along their zigzag edge make a class of materials [33]. Throughout this paper, these zigzag-edged LHs are referred to as $(ZrS_2)_m$-$(HfS_2)_n$, where the indices m and n represent the numbers of each kind of building constituent in the lateral primitive unit cell. The VHs are constructed from the stacking of single or a few ZrS_2 and HfS_2 layers, which are specified as $(ZrS_2)_m/(HfS_2)_n$. Because of the weak vdW interlayer interaction, the coupling between adjacent ZrS_2 and HfS_2 vertically stacked is rather weak, and it has small but crucial effects on the electronic structure [34]. The atomic configurations of the lateral and vertical heterostructures here proposed are sketched in Fig. 3 and Supplemental Material, Fig. S3 [35], respectively.

All the calculations are performed based on DFT in conjunction with the projector augmented-wave (PAW) potentials [36] implemented by the Vienna *Ab initio* Simulation Package (VASP) code [37]. The exchange-correlation energy is described by the generalized gradient approximation using the Perdew-Burke-Ernzerhof (PBE) functional [38]. The periodic in-plane and out-plane hybridized layers are optimized within one repeating unit. The kinetic energy cutoff for the plane-wave basis set was chosen to be 500 eV and the convergence criteria for energy and force are set to be 10^{-5} and 0.01 eV/Å, respectively. We used the conjugate gradient method for optimizing the atomic positions, interlayer spacings, and lattice constants. Brillouin zones were sampled using the Monkhorst-Pack scheme [39] where the Gamma-centered k-point mesh is employed according to the size of unit cells in the direct space. The number of the k points along the in-plane periodic direction was determined by the smallest integer that fulfills $n_k L = 30$ Å, where L is the lattice constant of the supercell in the periodic direction. DFT-D2 method is applied to describe the long-range vdW interaction [40] for the VHs, which is important in determining the geometric and electronic properties. The LHs and finite VHs are repeated periodically along the z direction; a vacuum spacing of 18 Å is introduced to avoid possible interactions between adjacent layers and their periodic images. Optical properties are some of the most important properties for a material, indicating a material's response to electromagnetic radiation. To model the optical response of the ZrS_2-HfS_2 heterostuctures, the complex dielectric function, $\varepsilon(\omega) = \varepsilon_1(\omega) + i\varepsilon_2(\omega)$, is calculated. The dielectric function provides a fundamental insight for evaluating further optoelectronic applications, since it connects the macroscopic properties with the microscopic band structure. The frequency- or energy-dependent dielectric function consists mainly of interband contributions for a semiconductor. The frequency-dependent dielectric matrix contains the imaginary part of dielectric constants $\varepsilon_2(\omega)$ in PAW methodology that would be obtained after the electronic ground state is determined [41]. Then the real part of the dielectric function can be obtained by the usual Kramers-Kronig transformation [42].

III. RESULTS AND DISCUSSION

A. Electronic properties

The 1*T*-ZrS_2 and 1*T*-HfS_2 consist of a layer of Zr (Hf) atoms sandwiched between two layers of S atoms with the Zr (Hf) atom octahedrally coordinated with the chalcogen one as shown in Fig. 1. The intralayer Zr (Hf)–S bonding is strong

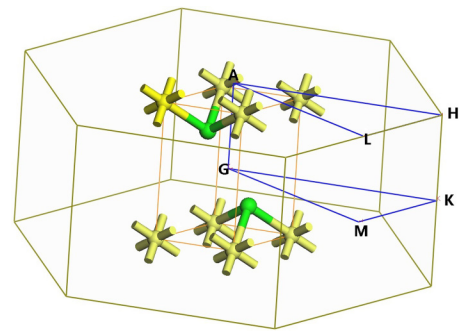

FIG. 1. Brillouin zone with high-symmetry k points used in band-structure calculations, where 1*T*-MX_2 (M = Zr, Hf; X = S) unit-cell structure is also shown; the green and yellow spheres denote M and S atoms, respectively.

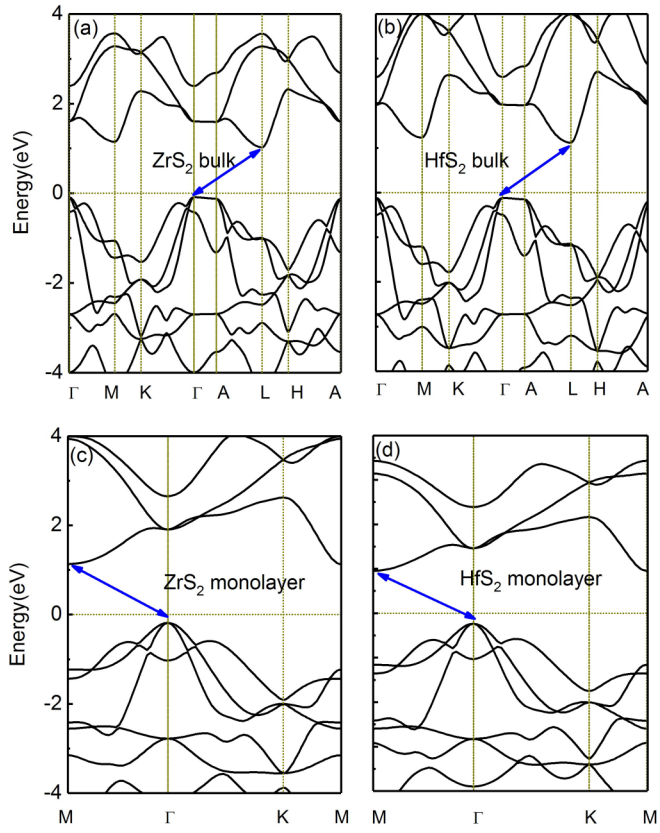

FIG. 2. Band structures of bulk ZrS_2, bulk HfS_2, ZrS_2 monolayer, and HfS_2 monolayer. The blue arrows indicate the band gaps and the horizontal dashed lines represent the Fermi level.

while the interlayer bonding is weak as it arises from vdW interaction. 1*T*-ZrS_2 and 1*T*-HfS_2 are all semiconductors and the band gaps fall in the range of the visible infrared region, thus being promising candidates for photovoltaic applications [14]. The calculated lattice constants of bulk (monolayer) ZrS_2 and HfS_2 are $a = b = 3.6822$ Å and $a = b = 3.642$ Å (3.6821 and 3.643 Å), respectively, agreeing well with previous studies [33,43]. The lattice mismatch of ZrS_2 and HfS_2 is merely 1.0%, implying that it is very suitable to build VHs and LHs based upon these two materials. For a better understanding of the electronic properties and the dielectric function of the ZrS_2/HfS_2 heterostructsures, it is useful to study the electronic structures of bulks and monolayer ZrS_2 and HfS_2. It is known that there is some difference in Brillouin zones of bulk and monolayer structures. The Brillouin zones with high-symmetry k points used in band-structure calculations are illustrated in Fig. 1. As can be seen in Figs. 2(a) and 2(b), the band gaps of bulk ZrS_2 and HfS_2 are both found to be indirect with values of 1.112 and 1.238 eV at PBE level, respectively, The valence-band maximum (VBM) and conduction-band minima (CBM) of the pristine bulk ZrS_2 and HfS_2 are located at Γ and L points, respectively. Figures 2(c) and 2(d) are the band structures of the monolayer ZrS_2 and HfS_2. Clearly, they also belong to indirect band-gap semiconductors with band gaps of 1.186 and 1.316 eV, respectively. Their CBM at Γ and VBM are at M points; this feature is different from some other TMDs such as MoS_2, WS_2, etc., which undergo a

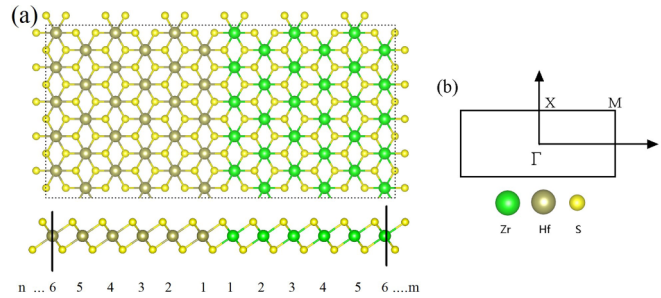

FIG. 3. Top and side views of atomic configurations of $(ZrS_2)_m$-$(HfS_2)_n$ lateral heterostructure monolayers with zigzag interlines, where $m = 6$ and $n = 6$. Green, sand, and yellow balls indicate Zr, Hf, and S atoms, respectively. (b) 2D Brillouin zone of the monolayer LH with high-symmetry points.

transition from an indirect to direct-gap semiconductor when their thickness is thinned down to a single layer [44].

Lateral and vertical heterostructures made of 2D single layer like graphene/*h*-BN [45] or MoS_2/WS_2 [10] have been previously studied, both theoretically and experimentally, motivating the construction of composite materials with promising applications. The 1*T*-ZrS_2 and 1*T*-HfS_2 monolayers reported here possess hexagonal symmetry and a sandwichlike structure, with close lattice constants values. The similar geometric structures and lattice parameters of ZrS_2 and HfS_2 will be beneficial in experimental fabrications. Based on the structural characteristics, two different types of LHs can be established with zigzag and with armchair types of interlines. The $(ZrS_2)_m$-$(HfS_2)_n$ LHs with zigzag interlines are thermally and dynamically stable; the stable properties can be seen from the phonon dispersion and the molecular-dynamic simulation as shown in Figs. S1(a) and S1(b) (see the Supplemental Material [35]). The frequencies of all phonon branches in the entire Brillouin zone are positive and the variation of free energy only shows slight oscillation even at 500 K, while the $(ZrS_2)_m$-$(HfS_2)_n$ LHs with armchair interlines are dynamically instable [33]. Therefore, in this paper we just focus on the $(ZrS_2)_m$-$(HfS_2)_n$ LHs with zigzag interlines. Figure 3(a) shows the typical atomic structures of the zigzag LHs $(ZrS_2)_m$-$(HfS_2)_n$, where $m = n = 6$ are the numbers of formula units in the lateral primitive unit cell. The green, sand, and yellow balls indicate Zr, Hf, and S atoms, respectively. Along the y direction of the lateral heterostructures shown in Fig. 3(a), the monolayer ZrS_2 and HfS_2 extend to infinity. The x direction is perpendicular to the zigzag edges, along which two different stripes repeat alternately and periodically. In the xy plane, the heterostructure has a 2D rectangular lattice and each constituent consists of three parallel atomic planes, where the plane of metal atoms (Zr or Hf) is capped by two S atomic planes. The lateral heterostructures are repeated periodically along the z direction with a vacuum spacing of 18 Å in a three-dimensional (3D) orthorhombic lattice. The proposed structure is similar to the previous *h*-BN/graphene, MoS_2/WS_2, and As/Sb-based LHs [45–47]. Figure 3(b) shows the 2D Brillouin zone of the monolayers with high-symmetry points.

Among the lateral heterostructures, we first study the electronic structure of the $(ZrS_2)_1$-$(HfS_2)_1$ LH with zigzag

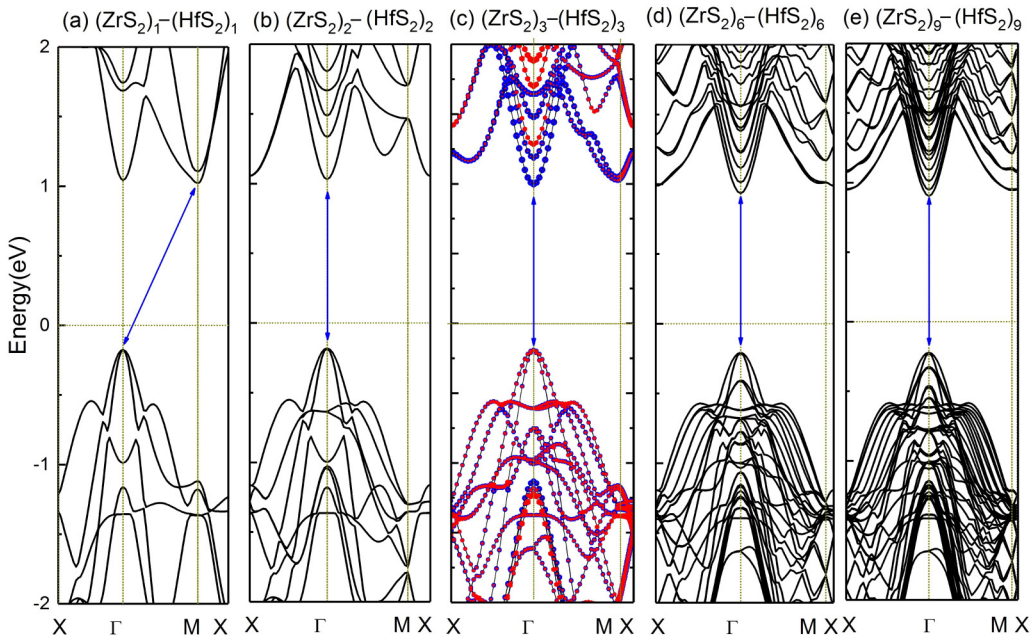

FIG. 4. Calculated band structures of the periodic lateral heterostructures $(ZrS_2)_m$-$(HfS_2)_n$ at PBE level. (a) $(ZrS_2)_1$-$(HfS_2)_1$, (b) $(ZrS_2)_2$-$(HfS_2)_2$, (c) $(ZrS_2)_3$-$(HfS_2)_3$, (d) $(ZrS_2)_6$-$(HfS_2)_6$, and (e) $(ZrS_2)_9$-$(HfS_2)_9$, where (c) is the calculated projected band structure; the blue and red lines represent the ZrS_2 and HfS_2 components of the bands, respectively. The blue arrows indicate the band gaps and the horizontal dashed lines represent the Fermi level.

interline, which is a composite structure constructed of very narrow stripes. As can be seen from the corresponding band structure plotted in Fig. 4(a), the $(ZrS_2)_1$-$(HfS_2)_1$ LH is a semiconductor with an indirect gap of 1.195 eV. In order to gain comprehensive information about $(ZrS_2)_m$-$(HfS_2)_n$ LHs, the size of building stripes is further increased. In Figs. 4(b)–4(e), we show the corresponding band structures of $(ZrS_2)_2$-$(HfS_2)_2$, $(ZrS_2)_3$-$(HfS_2)_3$, $(ZrS_2)_6$-$(HfS_2)_6$, and $(ZrS_2)_9$-$(HfS_2)_9$ LHs, respectively. An obvious common feature of this compound is its direct band gap, with the VBM and CBM both located at the Γ point, displaying a rather different behavior from those of pristine bulk (monolayer) ZrS_2 and HfS_2 as well as $(ZrS_2)_1$-$(HfS_2)_1$. At PBE level, the calculated band gaps of $(ZrS_2)_2$-$(HfS_2)_2$, $(ZrS_2)_3$-$(HfS_2)_3$, $(ZrS_2)_6$-$(HfS_2)_6$, and $(ZrS_2)_9$-$(HfS_2)_9$ LHs are 1.212, 1.188, 1.143, and 1.125 eV, respectively. There is a monotonous trend in the band gap of $(ZrS_2)_m$-$(HfS_2)_n$ LHs, which decreases gradually as the width of ZrS_2 and HfS_2 constituents increase. To further check the direct nature, we also perform calculations at the more accurate but computationally expensive hybrid functional level [48]. As shown in Fig. S2(a), the band gap of $(ZrS_2)_3$-$(HfS_2)_3$ LH is 2.008 eV under the hybrid HeydScuseria-Ernzerhof functional (HSE06) correction, which also clearly suggests a direct band-gap feature for $(ZrS_2)_3$-$(HfS_2)_3$ LH. We found that the HSE functional only enlarges the band gaps moderately compared with the PBE but does not change the trend of the electronic structures. Although the quantitative accuracy is subject to some uncertainty, DFT methods are still powerful for predicting a correct trend and related physical mechanisms.

To discuss the origination of the indirect-direct band-gap transition, we compare the two Brillouin zones shown in Fig. 1 and Fig. 3(b). It is found that the high-symmetry k points Γ and M of the hexagonal phase would be folded into the Γ point in the Brillouin zone of the rectangular supercell phase, thereby rendering ZrS_2 with its rectangular supercell structure $(ZrS_2)_2$-$(ZrS_2)_2$ as a (pseudo)-direct band-gap material as shown in the left panel of Fig. S2(b). For the sake of comparison, the band structures of $(ZrS_2)_2$-$(HfS_2)_2$ are also plotted. We identify that band-folding effect plays a critical role to produce the direct band gaps in the proposed LHs. In order to understand the electronics structures of the LHs, the projected band structures of $(ZrS_2)_3$-$(HfS_2)_3$ are plotted in Fig. 4(c). It is clear that the conduction band and the valence band mainly consist of states from ZrS_2 and HfS_2, respectively, indicating the type-II heterostructure. The type-II band alignment could also be the reason for the transition from indirect to direct semiconductor in the LHs [33]. The plane-averaged electron density difference along the direction perpendicular to the 1D boundary and the charge-density difference of the interface region are plotted in in Fig. S2(c) to illustrate the bonding feature and charge transfer at the interface. It is found that the charge redistribution mainly involves the atoms near the 1D interface, where certain electrons transfer happens between the HfS_2 and ZrS_2 monolayer. In the LHs, the charge transfer is mainly related to the building components, as well as the interline between HfS_2 and ZrS_2, leading to the presented orbital structure of bands in LHs.

Besides the lateral heterostructures, we also investigate two kinds of vertical heterostructures $(ZrS_2)_m/(HfS_2)_n$ composed of m-layer ZrS_2 and n-layer HfS_2, which are vertically and commensurately stacked. The first one is a V-infinite heterostructure composed of m-layer ZrS_2 and n-layer HfS_2 as shown in the inset of Fig. 5(a); this stacking sequence repeats periodically and continuously with a 3D hexagonal lattice. The second one is a V-finite heterostructure composed

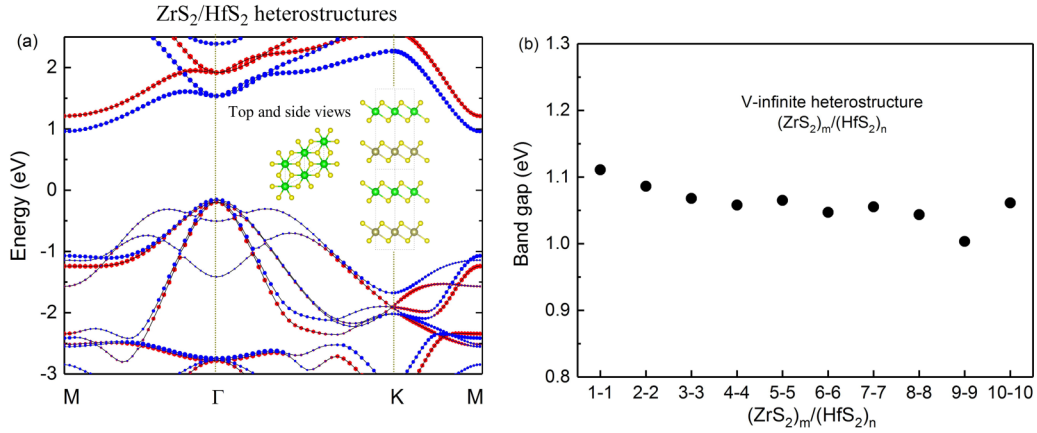

FIG. 5. Calculated projected band structure of the *V*-infinite heterostructures $(ZrS_2)_1/(HfS_2)_1$; the top and side views of the *AA* stacking heterostructure are shown in the inset. (b) The band gap of different *V*-infinite heterostructures $(ZrS_2)_m/(HfS_2)_n$, where $m = n$ is an integer.

of $m\,ZrS_2$ layers continued vertically by a stack of $n\,HfS_2$ layers. Since there are two possible stacking ways (*AA* and *AB*) to construct the $(ZrS_2)_m/(HfS_2)_n$ heterostructures (Fig. S3), we compare the total energies of the two *V*-infinite $(ZrS_2)_1/(HfS_2)_1$ heterostructures and find that *AA* stacking is more stable than *AB* stacking by about 35 meV. Therefore, we only focus on it in the following vertical heterostructure studies, which should be more preferred under experimental conditions. By changing the number of layers m and n of the constituent stacks, we can attain different heterostructures, which are also thermally and dynamically stable as shown in Figs. S1(c) and S1(d). Due to the same lattice symmetry of the monolayers and the ZrS_2/HfS_2 heterostructure, the Brillouin zone also remains unchanged [34]. Figure 5(a) shows the projected band structure of the *V*-infinite $(ZrS_2)_1/(HfS_2)_1$ heterostructure, where the curves highlighted by blue and orange circles are attributed to ZrS_2 and HfS_2 components, respectively. It is found that the *V*-infinite structure has an indirect band gap of 1.111 eV, which is smaller than both monolayers. It can be seen clearly that the band structures of the constituents are well maintained and separated, the band bending of ZrS_2 and HfS_2 in the heterostructure is small, and the vdW interactions between the ZrS_2/HfS_2 layers are weak. The band alignment manifests the intrinsic type-I heterostructure [34]. The band structures of the other *V*-infinite $(ZrS_2)_m/(HfS_2)_n$ heterostructures are also calculated; where $m = n$, it is found that all the *V*-infinite $(ZrS_2)_m/(HfS_2)_n$ heterostructures possess similar indirect gap nature, and the band gaps decrease very slightly with $m(n)$ and the gap nearly keeping about 1.05 eV as shown in Fig. 5(b).

In addition to the *V*-infinite $(ZrS_2)_m/(HfS_2)_n$ heterostructure with the same proportion of building blocks, we also study the $(ZrS_2)_m/(HfS_2)_n$ heterostructure with different ratios of components, that is, the boundaries have finite width but are asymmetric. In Fig. 6, the band structures of the asymmetric *V*-infinite heterostructures $(ZrS_2)_1/(HfS_2)_3$, $(ZrS_2)_1/(HfS_2)_5$, and $(ZrS_2)_1/(HfS_2)_7$ are illustrated. It is impressive that all the asymmetric structures are also indirect band-gap semiconductors, which are different from the lateral heterostructures $(ZrS_2)_m$-$(HfS_2)_n$ [33]. It is also interesting to note that the value of the energy gap is almost unchanged in the series of consecutive *V*-infinite heterostructures. The band gaps of the V-infinite heterostructures $(ZrS_2)_m/(HfS_2)_n$ are summarized in Table I. It is shown that there is not so much difference between the bulk materials and most of the considered heterostructures. This is mainly due to the fact that in the heterostructures the intrinsic tensile strain in HfS_2 and compressive strain in ZrS_2 are very small, where the lattices constant of the heterostructures, bulk ZrS_2 and HfS_2, are comparable as shown in Table I. While the external strains can provide an effective way to tune the electronic properties and thus enhance the performance of materials [49].

Here we consider the finite-size heterostructures composed of m-layer ZrS_2 stack continued vertically by a stack of n-layer HfS_2, specified as *V*-finite $(ZrS_2)_m/(HfS_2)_n$. Figure 7(a) shows the projected band structure of the *V*-finite structure ZrS_2/HfS_2; it is also found that the *V*-finite heterostructure has an indirect band gap (1.129 eV), where the red and blue circles represent the ZrS_2 and HfS_2 components of the bands, respectively. Figure 7(b) presents the calculated band structures of the other *V*-finite $(ZrS_2)_m/(HfS_2)_n$

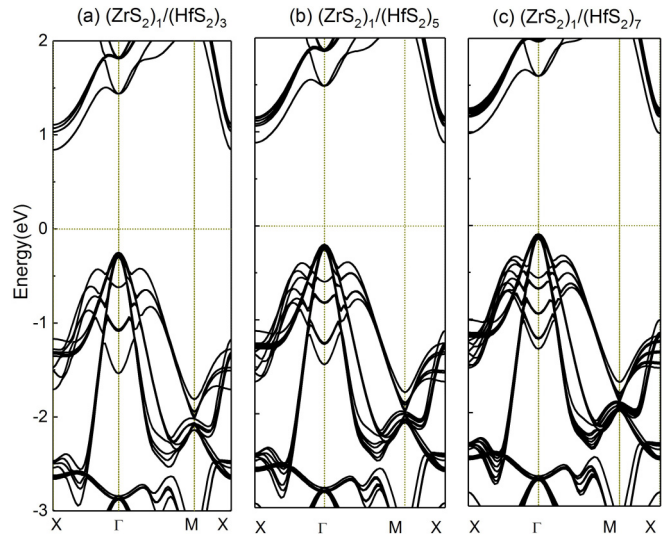

FIG. 6. Calculated band structures of the *V*-infinite heterostructures $(ZrS_2)_1/(HfS_2)_3$ (a), $(ZrS_2)_1/(HfS_2)_5$ (b), and $(ZrS_2)_1/(HfS_2)_7$ (c), respectively.

TABLE I. Lattice constants (a), band gaps, and hyperbolic dielectric properties of the V-infinite heterostructures $(ZrS_2)_m/(HfS_2)_n$. It is also found that all the V-infinite heterostructures keep the indirect band-gap property and possess a hyperbolic dielectric behavior.

Heterostructure $(ZrS_2)_m/(HfS_2)_n$	$m=1$ $n=1$	$m=1$ $n=3$	$m=1$ $n=5$	$m=2$ $n=2$	$m=3$ $n=3$	$m=4$ $n=4$	$m=5$ $n=5$	$m=6$ $n=6$	$m=7$ $n=7$	$m=8$ $n=8$	$m=9$ $n=9$	$m=10$ $n=10$
Lattice constant a (Å)	3.664	3.654	3.651	3.664	3.664	3.663	3.664	3.664	3.664	3.661	3.664	3.664
Band gap (eV)	1.111	1.0909	1.0821	1.0863	1.0681	1.0581	1.0652	1.0471	1.0553	1.0436	1.0034	1.0611
Hyperbolic window (eV)	0.2866	0.4218	0.4505	0.3067	0.2978	0.3083	0.2994	0.3166	0.3134	0.349	0.3548	0.3501

heterostructures, where $m=n$. It is found that all the $(ZrS_2)_m/(HfS_2)_n$ heterostructures possess similar indirect gap nature, and the band gaps decrease slightly with $m(n)$.

B. Optical properties

Our calculated band gaps of the bulk and the monolayer structures are in reasonable agreement with the reported calculated and experimental band gaps [5,50,51]. This suggests that we have a good starting point for the computation of the optical properties. From the dielectric constants, the other optical properties such as the absorption and reflection spectra can be calculated. Because of the sandwich layered properties, ZrS_2, HfS_2, and the heterostructures will show highly anisotropic mechanical, optical, and electrical properties [5]. Due to the anisotropy, the dielectric function perpendicular to the layer $\varepsilon_\perp$ is different from $\varepsilon_\parallel$ that is parallel to the layer. The real and imaginary parts of the energy-dependent dielectric functions are calculated at PBE level. All the imaginary parts of the dielectric function of the bulk, monolayer, and the heterostructures are calculated (not show here); in Fig. S4 we just show the imaginary parts of the dielectric function of the ZrS_2 bulk and monolayer. It is shown that the imaginary parts of $\varepsilon_\parallel$ dominate in the lower-energy region (0 to 4 eV); both $\varepsilon_\parallel$ and $\varepsilon_\perp$ contribute in the higher-energy region (above 4 eV).

The real part could be obtained through Kramers-Kronig relations [42]; the results of bulk ZrS_2, bulk HfS_2, monolayer ZrS_2, and monolayer HfS_2 are illustrated in Fig. 8. Strong anisotropy is observed between the real parts of dielectric functions $\varepsilon_\parallel$ and $\varepsilon_\perp$. It is found that the real part of $\varepsilon_\parallel$ of bulk ZrS_2(bulk HfS_2) is negative between 2.54 and 2.86 eV (2.74 and 3.30 eV), while $\varepsilon_\perp$ is positive, leading to a hyperbolic region [based on the criterion Real $(\varepsilon_\parallel)<0$)] in which the two components have different signs (marked as the blue shaded regions in Fig. 8). This sign difference is the characteristic feature of so-called indefinite media [18,19], which was proposed in the study of metamaterials and has important potential applications such as near-field focusing and spontaneous emission enhancement [20,21,52,53]. The bulk materials exhibit predominantly type-II dispersion corresponding to metallic response in plane and dielectric response out of plane [20]. The strong dielectric anisotropy should arise from the weak interlayer coupling that lowers carrier velocities and plasma frequencies perpendicular to the layers. For the monolayer ZrS_2 and monolayer HfS_2, they exhibit anisotropic dielectric properties. In order to predict accurate dielectric function, the HSE06 hybrid exchange-correlation functional is utilized to calculate the bulk ZrS_2. We compared the dielectric function of bulk ZrS_2 obtained with the PBE and HSE06 in Fig. S4(c), where the real parts of $\varepsilon_\parallel$ and $\varepsilon_\perp$

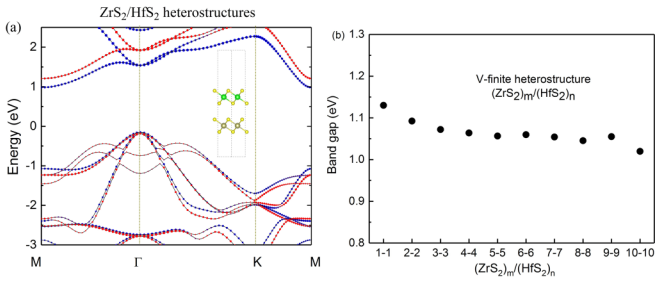

FIG. 7. Calculated projected band structure of the V-finite heterostructures $(ZrS_2)_1/(HfS_2)_1$ constructed by ZrS_2 and HfS_2 monolayer; the inset shows the side views of the AA stacking heterostructures. (b) Band gap of different V-finite heterostructures $(ZrS_2)_m/(HfS_2)_n$ formed by thin stacks of ZrS_2 and HfS_2.

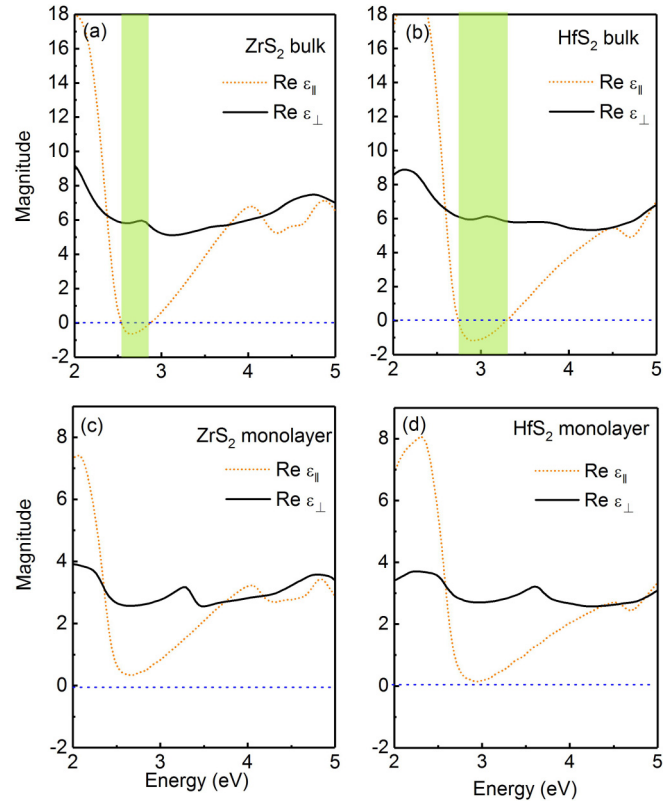

FIG. 8. Real parts of the two principal components of permittivity of bulk ZrS_2, bulk HfS_2, monolayer ZrS_2, and monolayer HfS_2, respectively, where $\varepsilon_\parallel$ represents in-plane component and $\varepsilon_\perp$ represents out-of-plane component. The shaded region shows the hyperbolic regions.

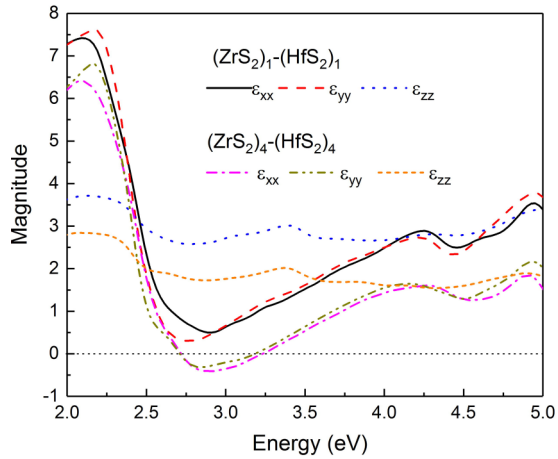

FIG. 9. Real parts of $\varepsilon_{\parallel}$ (ε_{xx},ε_{yy}) and $\varepsilon_{\perp}(\varepsilon_{zz})$ of the periodic lateral heterostructures $(ZrS_2)_1$-$(HfS_2)_1$ and $(ZrS_2)_4$-$(HfS_2)_4$, respectively.

are plotted. It is found that there are some blueshifts in the hyperbolic window from 2.54–2.86 eV (PBE) to 3.34–3.56 eV (HSE06) for ZrS_2 bulk. Although PBE calculation is expected to influence the precise position of the hyperbolic regions, the calculated results are reasonable to reflect the hyperbolic property. And, the more accurate methods such as the hybrid functional and DFT+U approach deserve to be investigated for the proposed heterostructures in future research.

For the lateral heterostructures, optical bianisotropy for in-plane and out-of-plane directions will be described by the dielectric tensor with three different components. $\varepsilon_{\parallel}(\varepsilon_{xx}$, $\varepsilon_{yy})$ and $\varepsilon_{\perp}(\varepsilon_{zz})$ of the periodic lateral heterostructure $(ZrS_2)_1$-$(HfS_2)_1$ and $(ZrS_2)_4$-$(HfS_2)_4$ are calculated in Fig. 9. It is found that lateral heterostructure $(ZrS_2)_1$-$(HfS_2)_1$ does not exhibit a hyperbolic region, while $(ZrS_2)_4$-$(HfS_2)_4$ possesses a hypobolic region between between 2.7 and 3.02 eV, where $\varepsilon_{xx} < 0$, $\varepsilon_{yy} < 0$ and $\varepsilon_{zz} > 0$. The metallic response in plane may come from the strong coupling between different constituents.

From the charge distribution and the charge-density difference in $(ZrS_2)_m/(HfS_2)_n$ VHs, it is found that the charges mainly distribute in the respective monolayer, whereas only a few charges will transfer at the interface. Hence, the dielectric response in the parallel direction can be determined by the respective material. Although the vdW interactions existing between the layers of the ZrS_2/HfS_2 heterostructure are weak, the interfaces play an important role in the scattering for electrons moving perpendicular to the interface and affect the perpendicular part of the optical dielectric functions. Figure 10(a) shows the calculated $\varepsilon_{\parallel}$ of the V-infinite heterostructures $(ZrS_2)_1/(HfS_2)_1$, $(ZrS_2)_3/(HfS_2)_3$, $(ZrS_2)_6/(HfS_2)_6$, and $(ZrS_2)_9/(HfS_2)_9$, where the shaded region shows the hyperbolic region. It is clear that all the V-infinite heterostructures possess a hyperbolic region between 2.7 and 3.02 eV. For comparison, we also calculated different

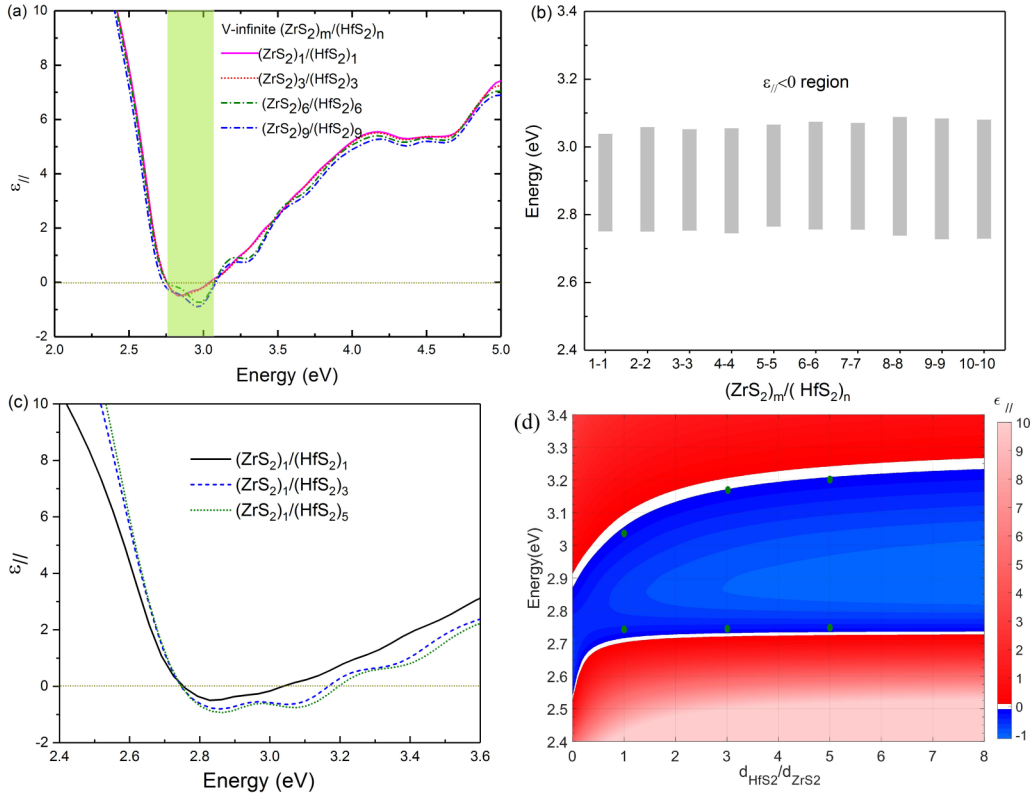

FIG. 10. $\varepsilon_{\parallel}$ of the V-infinite heterostructures $(ZrS_2)_1/(HfS_2)_1$, $(ZrS_2)_3/(HfS_2)_3$, $(ZrS_2)_6/(HfS_2)_6$, and $(ZrS_2)_9/(HfS_2)_9$ (a), where the shaded region shows the hyperbolic regions. (b) Hyperbolic regions of different V-infinite heterostructures $(ZrS_2)_m/(HfS_2)_n$. (c) $\varepsilon_{\parallel}$ of the V-infinite heterostructures $(ZrS_2)_1/(HfS_2)_3$ and $(ZrS_2)_1/(HfS_2)_5$; for comparison, $\varepsilon_{\parallel}$ of $(ZrS_2)_1/(HfS_2)_1$ is also plotted. (d) Effective $\varepsilon_{\parallel}$ of the composited ZrS_2/HfS_2 materials with different thickness ratios based on EMT, where the olive dots represent the calculated zeros of $\varepsilon_{\parallel}$ for $(ZrS_2)_1/(HfS_2)_1$, $(ZrS_2)_1/(HfS_2)_3$, and $(ZrS_2)_1/(HfS_2)_5$, respectively.

V-infinite heterostructures $(ZrS_2)_m/(HfS_2)_n$ with $m = n$ as shown in Fig. 10(b), it is found that when $m = n$, the hyperbolic regions are nearly the same. The hyperbolic character of the vertical heterostructure arise from the combination of the ZrS_2 and HfS_2, which is different from the dielectric property of the respective pristine ZrS_2 and HfS_2 bulk. Importantly, changes in the constituent ratio, *m/n*, result in tuning of the hyperbolic region. Figure 10(c) shows the calculated $\varepsilon_{\parallel}$ of the *V*-infinite heterostructures $(ZrS_2)_1/(HfS_2)_3$ and $(ZrS_2)_1/(HfS_2)_5$; the position and width of the hyperbolic region changes with the ratio of *m/n*. The hyperbolic dielectric properties of the *V*-infinite heterostructures $(ZrS_2)_m/(HfS_2)_n$ are summarized in Table I. To illustrate the degree of tuning that can be achieved by vdW heterostructures with different ZrS_2 and HfS_2 layers, we apply effective medium theory (EMT) to calculate the permittivity of the *V*-infinite heterostructures $(ZrS_2)_m/(HfS_2)_n$ with different thickness ratio, d_{HfS_2}/d_{ZrS_2}, where the thicknesses of the ZrS_2 and HfS_2 layers are sufficiently subwavelength. It should be noticed that the influence of hybridization at the interfaces and quantum confinement are neglected in this calculation [18].

In EMT, a uniaxial stratified periodic metamaterial consisting of ZrS_2 and HfS_2 layers can be characterized by the effective diagonal permittivity tensor $\varepsilon^{EMT} = \mathrm{diag}(\varepsilon_{//}^{EMT}, \varepsilon_{//}^{EMT}, \varepsilon_{\perp}^{EMT})$ with effective components given by [19] $\varepsilon_{//}^{EMT} = \rho \cdot \varepsilon_{//}^{HfS_2} + (1-\rho)\cdot\varepsilon_{//}^{ZrS_2}$, $1/\varepsilon_{\perp}^{EMT} = \rho/\varepsilon_{\perp}^{HfS_2} + (1-\rho)/\varepsilon_{\perp}^{ZrS_2}$, where $\rho = d_{HfS_2}/(d_{ZrS_2} + d_{HfS_2})$ is the fill fraction of HfS_2. Figure 10(d) shows that the hyperbolic energy region can be tunable, over which the heterostructure dispersion is hyperbolic. By choosing *V*-infinite heterostructures with different ZrS_2 and HfS_2 layers, the hyperbolic region can be adjusted. For comparison the calculated DFT data $\varepsilon_{\parallel}$ (for $(ZrS_2)_1/(HfS_2)_1$, $(ZrS_2)_1/(HfS_2)_3$, and $(ZrS_2)_1/(HfS_2)_5$] are also plotted in Fig. 10(d). The *V*-infinite heterostructures are hyperbolic in the ranges 2.750–3.038 eV, 2.745–3.168 eV, and 2.745–3.197 eV, respectively, which are in good agreement with the EMT results. For the TMDs heterostructure-based HMMs, EMT can be effective in evaluating the hyperbolic regime where real($\varepsilon_{\parallel}$)<0. Further tuning is obviously possible by considering heterostructures with other 2D material or metal [52]. In addition, the hyperbolic dispersion properties are also found in the *V*-finite heterostructures $(ZrS_2)_m/(HfS_2)_n$. In the hyperbolic region, the surfaces of constant frequency are hyperbolic, extending to very large values of wave vector. Because of the momentum mismatch, the naturally HMMs will possess large local density of states [21,53] and are expected to deliver high Purcell enhancements.

C. Purcell enhancement

One of the most promising applications of hyperbolic metamaterials is spontaneous emission engineering, which plays a crucial role in single-photon sources and light-emission devices [21,54]. Due to the hyperbolic dispersion, a dipole emitter can couple to a large range of wave vector states at a single frequency, thereby increasing the number of possible decay paths. The Purcell factor is generally defined as the ratio of the radiative rate in a particular electromagnetic structure to that in vacuum; it is an efficient parameter to characterize the spontaneous emission properties, which describes the modification of the spontaneous emission lifetime [53]. In contrast to resonant structures like cavities or single-metallic interfaces, the HMMs exhibit a Purcell factor that is broadband and tunable in frequency [21]. To study the spontaneous emission enhancement of a point source above such $(ZrS_2)/(HfS_2)$ multilayer HMMs, Purcell factors are computed. For simplicity an ideal electric dipole with internal quantum efficiency $q_0 = 1$ is adopted. When a dipole is placed at a distance of d above the planar HMM with polarization perpendicular ($\perp$) or parallel ($\parallel$) to the interface, the corresponding Purcell factors can be written as [53,55] $F_{p\perp} = 1 - q_0 + \frac{3}{2}q_0\mathrm{Re}\int_0^{\infty}\frac{1}{k_z}(\frac{k_x}{\sqrt{\varepsilon_1}k_0})^3(1 + r_p e^{2ik_z d})dk_x$ and $F_{p\perp} = 1 - q_0 + \frac{3}{4}q_0\mathrm{Re}\int_0^{\infty}\frac{1}{k_z}\frac{k_x}{\sqrt{\varepsilon_1}k_0}[1 + r_s e^{2ik_z d} + \frac{k_z^2}{\varepsilon_1 k_0^2}(1 - r_p e^{2ik_z d})dk_x$, where k_0 is the magnitude of the wave vector in a vacuum, ε_1 is the relative permittivity for the host material which contains fluorescent emitters such as quantum dots and dye molecules, k_x and $k_z = \sqrt{\varepsilon_1 k_0^2 - k_x^2}$ are the wave-vector components along the in-plane and vertical directions, respectively, and $r_{p,s}$ is the

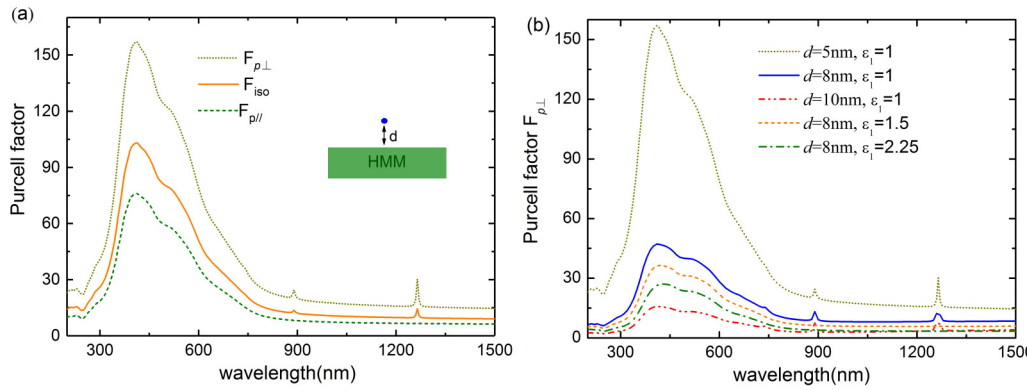

FIG. 11. (a) Purcell factor for the dipoles perpendicular ($F_{p\perp}$, short dotted line) and parallel ($F_{p//}$, short dashed line) to the surface as depicted in the insets (the blue dot represents a dipole); the solid line represents the Purcell factor F_{iso} for an isotropic dipole which is averaged from $F_{p\perp}$ and $F_{p//}$. The dipole is in air 5 nm above the $(ZrS_2)/(HfS_2)$ multilayer HMM with $d_{HMM} = 20$ nm. (b) Purcell factor $F_{p\perp}$ as a function of wavelength with different d and ε_1.

reflection coefficient at the interfaces for a TM (TE) polarized wave, which can be calculated by transfer matrix method [56]. The isotropic Purcell factor $F_{\rm iso}$ can be obtained through an average over $F_{p\perp}$ and $F_{p//}$, that is, $F_{\rm iso} = \frac{1}{3}F_{p\perp} + \frac{2}{3}F_{p//}$, where the factor 2 accounts for the two equivalent orthogonal in-plane orientations.

Figure 11(a) shows the Purcell factor for the dipoles perpendicular ($F_{p\perp}$, short dotted line) and parallel ($F_{p//}$, short dashed line) to the *V*-infinite $(ZrS_2)/(HfS_2)$ heterostructure surface with $d_{\rm HMM} = 20$ nm as depicted in the inset; the solid line represents the Purcell factor $F_{\rm iso}$ for an isotropic dipole which is averaged from $F_{p\perp}$ and $F_{p//}$. The distance between dipole and the $(ZrS_2)/(HfS_2)$ heterostructure HMM is $d = 5$ nm and $\varepsilon_1 = 1$. The permittivity of the naturally HMM calculated by DFT is shown in Fig. S5, around 450 nm, where $\varepsilon_{//} < 0$, the dispersion relation, is hyperbolic. The peak of the Purcell factor is located at the 300–650-nm wavelength region which might result from the larger local density of states around the hyperbolic region, and the Purcell factor $F_{p\perp}$ is much higher than $F_{p//}$. About 102-fold enhancement at $\lambda = 405$ nm is obtained. Figure 11(b) shows the Purcell factor $F_{p\perp}$ as a function of wavelength with different d and ε_1. Apparently, the Purcell factor relates to the distance between the dipole and the $(ZrS_2)/(HfS_2)$ heterostructure and the host materials. The Purcell factor decreases with the coupling distance d and the permittivity of the host materials.

IV. CONCLUSION

In summary, we have studied the electronic and optical dielectric properties of the lateral and vertical heterostructures composed of ZrS_2 and HfS_2 mono- and multilayer. It is found that both the monolayer and the bulk structures are intrinsic indirect semiconductors, while the lateral heterostructures $(ZrS_2)_m$-$(HfS_2)_n$ exhibit an indirect to direct band-gap transition. The optical properties of the HfS_2 and ZrS_2 bulk and monolayers are found to be strongly anisotropic. The bulk HfS_2 and ZrS_2 are naturally hyperbolic metamaterial between 2.54 and 2.86 eV (2.74 and 3.30 eV), respectively. The periodic and finite-size vertical heterostructures $(ZrS_2)_m/(HfS_2)_n$ keep the indirect band-gap property. The vertical heterostructures possess tunable hyperbolic dielectric behavior and the property can be well predicted by the effective medium theory, where the interface effects are not crucial, while the heterostructures with non-negligible interface effects deserve to be investigated as the next step. Furthermore, in the hyperbolic region, over a 100-fold Purcell factor enhancement is obtained, presenting a promising opportunity for the realization of hyperbolic metamaterial-based devices for light generation.

ACKNOWLEDGMENTS

L.Z. would like to thank Dr. P. Cencillo-Abad at NanoScience Technology Center, University of Central Florida (USA) for helpful advice in revising this paper. This research was supported by National Natural Science Foundation of China (Grants No. U1804165, No. U1604133, No. 11804081, and No. 11804082) and by Natural Science Foundation of Henan Province (Grants No. 15A416007, No. NSFRF140132, and No. 182102410047).

[1] S. Manzeli, D. Ovchinnikov, D. Pasquier, O. V. Yazyev, and A. Kis, Nat. Rev. Mater. **2**, 17033 (2017).
[2] P. Liu and B. Xiang, Sci. Bull. **62**, 1148 (2017).
[3] S. Dai, Q. Ma, M. Liu, T. Andersen, Z. Fei, M. Goldflam, M. Wagner, K. Watanabe, T. Taniguchi, and M. Thiemens, Nat. Nanotechnol. **10**, 682 (2015).
[4] A. A. Tedstone, D. J. Lewis, and P. O'Brien, Chem. Mater. **28**, 1965 (2016).
[5] Q. Zhao, Y. Guo, K. Si, Z. Ren, J. Bai, and X. Xu, Phys. Status Solidi B **254**, 1700033 (2017).
[6] W. Choi, N. Choudhary, G. H. Han, J. Park, D. Akinwande, and Y. H. Lee, Mater. Today **20**, 116 (2017).
[7] F. Zheng and J. Feng, Phys. Rev. B **99**, 161119(R) (2019).
[8] A. K. Geim and I. V. Grigorieva, Nature (London) **499**, 419 (2013).
[9] Z. Ji, H. Hong, J. Zhang, Q. Zhang, W. Huang, T. Cao, R. Qiao, C. Liu, J. Liang, and C. Jin, ACS Nano **11**, 12020 (2017).
[10] Z. Wang, Y. Xie, H. Wang, R. Wu, T. Nan, Y. Zhan, J. Sun, T. Jiang, Y. Zhao, and Y. Lei, Nanotechnology **28**, 325602 (2017).
[11] H. Taghinejad, A. A. Eftekhar, and A. Adibi, Opt. Mater. Express **9**, 1590 (2019).
[12] E. Pomerantseva and Y. Gogotsi, Nat. Energy **2**, 17089 (2017).
[13] V. D. S. O. Ganesan, J. Linghu, C. Zhang, Y. P. Feng, and L. Shen, Appl. Phys. Lett. **108**, 122105 (2016).
[14] L. Li, H. Wang, X. Fang, T. Zhai, Y. Bando, and D. Golberg, Energy Environ. Sci. **4**, 2586 (2011).
[15] M. Zhang, Y. Zhu, X. Wang, Q. Feng, S. Qiao, W. Wen, Y. Chen, M. Cui, J. Zhang, C. Cai, and L. Xie, J. Am. Chem. Soc. **137**, 7051 (2015).
[16] T. Kanazawa, T. Amemiya, A. Ishikawa, V. Upadhyaya, K. Tsuruta, T. Tanaka, and Y. Miyamoto, Sci. Rep.-UK **6**, 22277 (2016).
[17] A. Onen, D. Kecik, E. Durgun, and S. Ciraci, J. Phys. Chem. C **121**, 27098 (2017).
[18] M. N. Gjerding, R. Petersen, T. Pedersen, N. A. Mortensen, and K. S. Thygesen, Nat. Commun. **8**, 320 (2017).
[19] A. Poddubny, I. Iorsh, P. Belov, and Y. Kivshar, Nat. Photonics **7**, 948 (2013).
[20] L. Ferrari, C. H. Wu, D. Lepage, X. Zhang, and Z. W. Liu, Prog. Quantum Electron. **40**, 1 (2015).
[21] D. Lu, J. J. Kan, E. E. Fullerton, and Z. Liu, Nat. Nanotechnol. **9**, 48 (2014).
[22] Y.-L. Liao, Y. Zhao, S. Wu, and S. Feng, Opt. Mater. Express **8**, 2484 (2018).
[23] A. P. Slobozhanyuk *et al.*, Phys. Rev. B **92**, 195127 (2015).
[24] O. Kidwai, S. V. Zhukovsky, and J. E. Sipe, Phys. Rev. A **85**, 053842 (2012).
[25] P. Shekhar, S. Pendharker, D. Vick, M. Malac, and Z. Jacob, Opt. Express **27**, 6970 (2019).

[26] J. D. Caldwell, A. V. Kretinin, Y. Chen, V. Giannini, M. M. Fogler, Y. Francescato, C. T. Ellis, J. G. Tischler, C. R. Woods, and A. J. Giles, Nat. Commun. **5**, 5221 (2014).
[27] E. E. Narimanov and A. V. Kildishev, Nat. Photonics **9**, 214 (2015).
[28] Z. Liu and K. Aydin, Nano Lett. **16**, 3457 (2016).
[29] H. Qi, L. Wang, J. Sun, Y. Long, P. Hu, F. Liu, and X. He, Crystals **8**, 35 (2018).
[30] R. Dong and I. Kuljanishvili, J. Vac. Sci. Technol. B **35**, 030803 (2017).
[31] K. Novoselov, A. Mishchenko, A. Carvalho, and A. C. Neto, Science **353**, aac9439 (2016).
[32] A. Onen, D. Kecik, E. Durgun, and S. Ciraci, Phys. Rev. B **95**, 155435 (2017).
[33] J. Yuan, N. Yu, J. Wang, K.-H. Xue, and X. Miao, Appl. Surf. Sci. **436**, 919 (2018).
[34] J. Shang, S. Zhang, X. Cheng, Z. Wei, and J. Li, RSC Adv. **7**, 14625 (2017).
[35] See Supplemental Material at http://link.aps.org/supplemental/10.1103/PhysRevB.100.165304 for the phonon dispersion and the molecular dynamics of the lateral heterostructure and vertical heterostructure, the band structures of $(ZrS_2)_3$-$(HfS_2)_3$ and the superlattice $(ZrS_2)_2$-$(ZrS_2)_2$, and the dielectric functions of the ZrS_2 bulk, monolayer, and *V*-infinite $(ZrS_2)/(HfS_2)$ heterostructure.
[36] P. E. Blöchl, Phys. Rev. B **50**, 17953 (1994).
[37] G. Kresse and J. Furthmüller, Phys. Rev. B **54**, 11169 (1996).
[38] J. P. Perdew, K. Burke, and M. Ernzerhof, Phys. Rev. Lett. **77**, 3865 (1996).
[39] H. J. Monkhorst and J. D. Pack, Phys. Rev. B **13**, 5188 (1976).
[40] S. Grimme, J. Comput. Chem. **27**, 1787 (2006).
[41] M. Gajdoš, K. Hummer, G. Kresse, J. Furthmüller, and F. Bechstedt, Phys. Rev. B **73**, 045112 (2006).
[42] V. Lucarini, J. J. Saarinen, K.-E. Peiponen, and E. M. Vartiainen, *Kramers-Kronig Relations in Optical Materials Research* (Springer Science & Business Media, Berlin, 2005).
[43] Y. Li, J. Kang, and J. Li, RSC Adv. **4**, 7396 (2014).
[44] A. Kumar and P. Ahluwalia, Eur. Phys. J. B **85**, 186 (2012).
[45] Q. Sun, Y. Dai, Y. Ma, W. Wei, and B. Huang, RSC Adv. **5**, 33037 (2015).
[46] Q. Wang, P. Wu, G. Cao, and M. Huang, J. Phys. D: Appl. Phys. **46**, 505308 (2013).
[47] Q. Sun, Y. Dai, Y. Ma, N. Yin, W. Wei, L. Yu, and B. Huang, 2D Mater. **3**, 035017 (2016).
[48] J. Heyd, G. E. Scuseria, and M. Ernzerhof, J. Chem. Phys. **118**, 8207 (2003).
[49] H. Guo, N. Lu, L. Wang, X. Wu, and X. C. Zeng, J. Phys. Chem. C **118**, 7242 (2014).
[50] Y. Zhu, X. Wang, M. Zhang, C. Cai, and L. Xie, Nano Res. **9**, 2931 (2016).
[51] F. A. Rasmussen and K. S. Thygesen, J. Phys. Chem. C **119**, 13169 (2015).
[52] X. Song, Z. Liu, Y. Xiang, and K. Aydin, Opt. Express **26**, 5469 (2018).
[53] L. Li, W. Wang, T. S. Luk, X. Yang, and J. Gao, ACS Photonics **4**, 501 (2017).
[54] S. Axelrod, M. K. Dezfouli, H. M. K. Wong, A. S. Helmy, and S. Hughes, Phys. Rev. B **95**, 155424 (2017).
[55] G. W. Ford and W. H. Weber, Phys. Rep. **113**, 195 (1984).
[56] L. Zhang, W. Yu, J.-Y. Ou, Q. Wang, X. Cai, B. Wang, X. Li, R. Zhao, and Y. Liu, Phys. Rev. B **98**, 075434 (2018).